Water surface slope spectra in nearshore and river mouth environments

Water surface slope spectra in nearshore and river mouth environments

N J M Laxague, D G Ortiz-Suslow, B K Haus, N J Williams and H C Graber

University of Miami, Rosenstiel School of Marine and Atmospheric Science, Department of Ocean Sciences, 4600 Rickenbacker Causeway, Miami, FL 33149, USA

E-mail: nlaxague@rsmas.miami.edu

Abstract. With the ever-growing interest in satellite remote sensing, direct observations of short wave characteristics are needed along coastal margins. These zones are characterized by a diversity of physical processes that can affect sea surface topography. Here we present connections made between ocean wave spectral shape and wind forcing in coastal waters using polarimetric slope sensing and eddy covariance methods; this is based on data collected in the vicinity of the mouth of the Columbia River (MCR) on the Oregon–Washington border. These results provide insights into the behavior of short waves in coastal environments under variable wind forcing; this characterization of wave spectra is an important step towards improving the use of radar remote sensing to sample these dynamic coastal waters. High wavenumber spectral peaks are found to appear for $U_{10} > 6$ m/s but vanish for $\tau > 0.1$ N/m^2, indicating a stark difference between how wind speed and wind stress are related to the short-scale structure of the ocean surface. Near-capillary regime spectral shape is found to be less steep than in past observations and to show no discernable sensitivity to wind forcing.

1. Introduction

In the study of physical processes and management of resources in coastal and nearshore environments, satellite radar remote sensing techniques are important and widely used tools. These techniques rely on back-scattering of transmitted radar signals by short ocean waves. Scattering models [1] depend upon the short ocean wave spectrum (i.e., decimeters and smaller — the range for which capillary effects become significant) in the determination of the normalized radar cross section (NRCS), or σ_0 — a quantity of primary importance for the retrieval of meteorological and oceanographic parameters from satellite images. The ability to accurately collect these parameters remotely is a powerful one — sea surface waves are of crucial significance to all manner of interactions between the atmosphere and ocean. Heat and gas fluxes are dramatically enhanced by the presence of ocean surface waves [2], holding implications for areas of study ranging from extreme storms to climatic processes. The transfer of momentum from the atmosphere into the ocean via wind forcing is inextricably connected to wind-wave growth, upper ocean mixing, and mass transport.

The vertical transfer of horizontal momentum from the atmosphere to the ocean (i.e., wind stress) is generally quantified using the eddy covariance method [3]. This relates the turbulent fluctuations in the wind velocity field to a characteristic wind velocity at the surface. Over water, it has long been established that these turbulent fluctuations are related to the small scale roughness features on the surface. Any process that affects the small scale surface waves ($\mathcal{O}(0.01 - 0.1)$ m) will modulate the atmospheric response to the surface [4].

There are a number of pitfalls associated with observing these short waves (even the 0.1-m waves are typically not sampled by buoys), especially outside of a controlled laboratory environment. Traditional time series observations are unable to properly isolate the effects of advection and Doppler-shifting of short waves by long waves [5]. For this reason, techniques that are able to retrieve synoptic, spatial measurements of wave structure are preferred for the study of short ocean waves [6]. The polarimetric slope sensing (PSS) technique is an optical method designed to accomplish such a task [7]; it has been used successfully to acquire short-scale wave structure from aboard a moving vessel [8, 9]. This has the advantage of adapting this relatively new field-ready technology to heterogeneous ocean surfaces where both spatial and temporal variability are first order concerns.

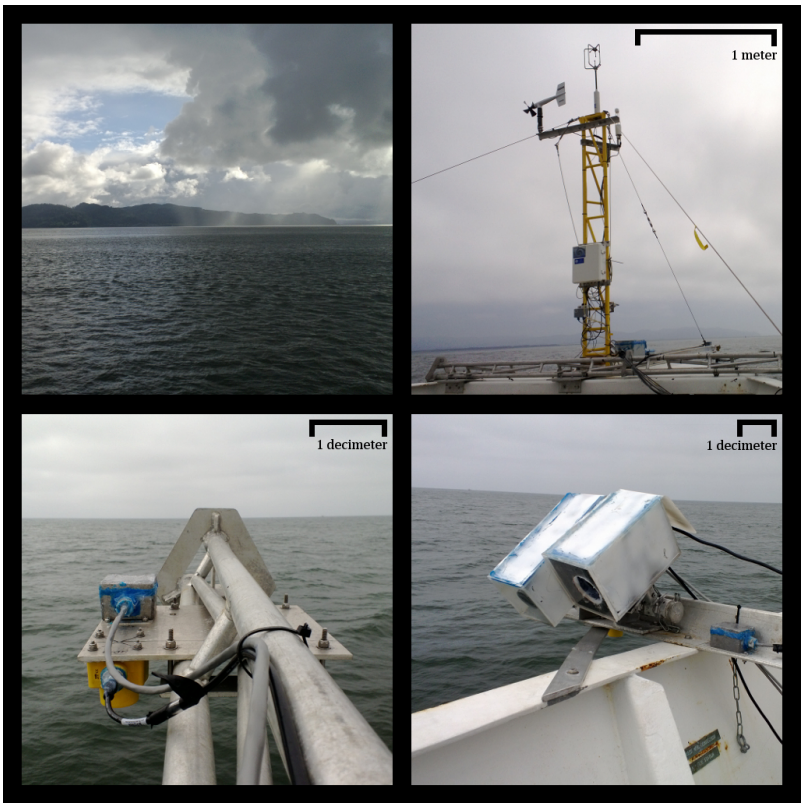

Figure 1. Images taken from and of the R/V *Point Sur*, clockwise from top left: view of the Washington coast from MCR; bow-mounted meteorological mast; starboard bow-mounted polarimetric and infrared cameras; starboard bow-mounted ultrasonic distance meter (UDM).

For this study, short wave and flux measurements aboard a research vessel were used. Field observations of wind stress and short scale wave slope were made in the vicinity of the Columbia River mouth aboard the R/V *Point Sur*. These observations were performed as part of the Office of Naval Research-sponsored Riverine and Estuarine Transport Experiment (RIVET) II. An over-arching goal of this multi-faceted campaign was to provide *in situ* observations of coastal wave-current-wind interaction that would improve efforts to use remote sensing platforms for sampling these dynamic regions. The work presented here furthers this aim by providing short wave observations fundamental to the acquisition methods of remote sensing sampling techniques.

2. Methods

2.1. Field observations: Mouth of the Columbia River

Observations were made at the mouth of the Columbia River (MCR) along the Oregon–Washington border from 25 May to 15 June 2013. The peak wave directions observed by NDBC buoy #46243 during the experimental time frame show waves generally incident from the west-northwest, with typical peak periods ranging from 7 to 12 s. Surface slope and wind stress measurements were made from the bow of the 135 foot R/V *Point Sur* (figure 1). A sonic anemometer was fastened atop a meteorological mast mounted (2.3 m from deck) on the bow providing three-dimensional wind velocities 8.1 m above the mean water level (MWL). A polarimetric camera was mounted off the starboard bow (figure 1) and oriented such that it was imaging an $\approx$1.56 m^2 region forward of the ship's wake zone. The vessel's angular and linear accelerations were logged at 20 Hz via a Systron-Donner six-axis motion package, which was located adjacent to the sensor suite on the ship's bow. This was used to motion-correct the flux measurements and to properly rectify the polarimeter frames. The following sections describe the methods used in retrieving the shipboard measurements of the wind stress and short wave slope spectra.

2.2. Wind stress: Eddy covariance

Given here is a condensed version of the estimation of wind stress via eddy covariance that is directly relevant to this study. The total stress vector on the ocean surface is generally taken as the covariance of the turbulent along- and across-wind velocities (u' and v') with the vertical wind component (w'),

$$\vec{\tau}_{wind} = -\rho_{air}\left[\langle u'w'\rangle\hat{x} + \langle v'w'\rangle\hat{y}\right] \tag{1}$$

where ρ_{air} is the air density and a prime indicates a turbulent quantity in a Reynolds decomposition (i.e., $\langle u'\rangle = \langle v'\rangle = \langle w'\rangle = 0$). The brackets indicate that a time average of the contained quantity has been computed over some appropriate interval. Simultaneous measurements of vessel motion enabled the 10-Hz winds measured from the sonic anemometer to be corrected for the vessel accelerations and translation [10]. Rejection criteria included averaging intervals with large vessel heading deviations ($\geq$40°) and winds coming from outside of $\pm$40°off the bow. Critical to the eddy covariance technique is the use of an appropriate averaging window, which can vary from study-to-study and platform-to-platform. Generally, intervals between 15 and 30 minutes are used in deep water conditions, where spatial homogeneity can be assumed over the sampling interval. A five-minute window was chosen for this study [11] due to the combination of the spatial heterogeneity of the wave and wind stress field observed at MCR and the area covered by the vessel ($\sim$ 1200 m per interval). It is expected that the short surface waves respond most directly to the smaller-scale eddies in the atmospheric boundary layer, which are fully resolved over this time frame. The U_{10} reported in this work is the 10-m, neutral wind speed calculated using the eddy covariance techniques, while the wind stress, τ, comes directly from the along- and across-wind covariance components of the Reynolds stress (equation 1).

2.3. Short waves: Polarimetric slope sensing

Following the work of Zappa *et al*. [2008], one may obtain the two-dimensional slope field $\vec{\sigma}(x,y)$ from a triplet of simultaneously-acquired images representing light intensities at 0°, 45°, and 90°polarization. The imaged area of the water surface spans 1.25 m by 1.25 m, with a minimally-resolvable (Nyquist) wavenumber of 1600 rad/m (corresponding to 3.9 mm). The primary simplifying assumptions for this work are that the incident light be unpolarized and the subsurface, upwelling light may be neglected. Multiple sky-looking acquisition runs showed that the light incident upon the surface was, in general, in an unpolarized state for the cases considered here. For the work presented here (as well as in Zappa *et al*. [2008]), upwelling light was taken to be negligible in general. The polarimeter frames were projectively

transformed onto the ocean surface in order to maintain a uniform scale across the image under a time-varying camera look angle [9].

$$\begin{aligned} S_0 &= I_0 + I_{90} \\ S_1 &= I_0 - I_{90} \\ S_2 &= 2 \cdot I_{45} - S_0 \end{aligned} \tag{2}$$

I_0, I_{45}, and I_{90} are the light intensities at 0°, 45°, and 90°, respectively. The Stokes parameters S_1 and S_2 are directly converted into the polarization orientation, from which follows the angle of intersection between the reflection and image planes. The tangent of this angle yields the slope in the cross-look direction.

$$\varphi = \frac{1}{2}\left[\pi + \tan^{-1}\left(\frac{S_2}{S_1}\right)\right], \qquad \sigma_y = \tan(\varphi) \tag{3}$$

In order to compute the slope in the along-look direction, the degree of linear polarization (DOLP) is generated using all three Stokes parameters (equation 4).

$$DOLP \quad = \quad \sqrt{\frac{S_1^2 + S_2^2}{S_0^2}} \quad = \quad \frac{r_\parallel^2 - r_\perp^2}{r_\parallel^2 + r_\perp^2} \tag{4}$$

$$r_\parallel = \frac{\tan(\theta_i - \theta_t)}{\tan(\theta_i + \theta_t)}, \quad r_\perp = \frac{\sin(\theta_i - \theta_t)}{\sin(\theta_i + \theta_t)} \tag{5}$$

$$\theta_i = n\sin(\theta_t), \quad \sigma_x = \tan(\theta_i) \tag{6}$$

The DOLP may alternatively be represented in terms of the Fresnel reflection coefficients (equation 4; defined in equation 5), which themselves depend upon the angle of incidence and the index of refraction n of water. Equation 6 describes the final step in producing a slope component from the observed angle of incidence. For this analysis, $n = 1.33$ was chosen based on an average water temperature and salinity of 14°C and 10 ppt, respectively; analysis of the *Point Sur* flow-through temperature and salinity data demonstrated that n should not have deviated more than 1% from this value for the duration of the experiment [12]. The focus of this work will be on the spectral properties of the time-averaged two-dimensional slope fields. Each scalar slope field $\|\vec{\sigma}(x,y)\|$ is subjected to a two-dimensional Fourier transform, yielding the two-dimensional slope spectrum $P(k_x, k_y)$. This may be integrated over direction to produce the omnidirectional slope spectrum $P(k)$. By multiplying $P(k)$ by k, one extracts the non-dimensional, omnidirectional saturation spectrum $B(k)$. The high-wavenumber regimes of this spectrum are emphasized; as such, it is often used to describe the short-wave behavior of the ocean surface. Empirical and theoretical wave spectra make fundamental use of the short-wave peak and post-peak behavior of $B(k)$ in defining spectral shape [13, 14]. $P(k)$ itself may be integrated with respect to wavenumber k to compute mean square slope ($\langle S^2 \rangle$ — literally, the mean of the squares of the slopes), an important statistical quantity used to represent surface roughness.

In the section of results that follows (section 3), references will be made to "inside-inlet" and "outside-inlet" data points. While it is difficult to set a hard line of demarcation between areas considered "inside" and "outside", the offshore edge of the south jetty at 124°6' W seemed to be the most reasonable separation point. From figure 2, one can indeed see that this is very nearly the westernmost magenta acquisition location. The separation of data between inside and outside-inlet groups provides a means of

comparing two different physical regimes where major differences in short wave statistics are expected. Sections 3 and 4 also refer to wavenumber regimes. These follow from and correspond to the relative values of the gravity and surface tension terms in the linear dispersion relation. They are: short gravity (37.1 rad/m $< k <$ 112.7 rad/m), gravity-capillary (112.7 rad/m $< k <$ 1173 rad/m), and pure capillary (1173 rad/m $< k <$ 1600 rad/m).

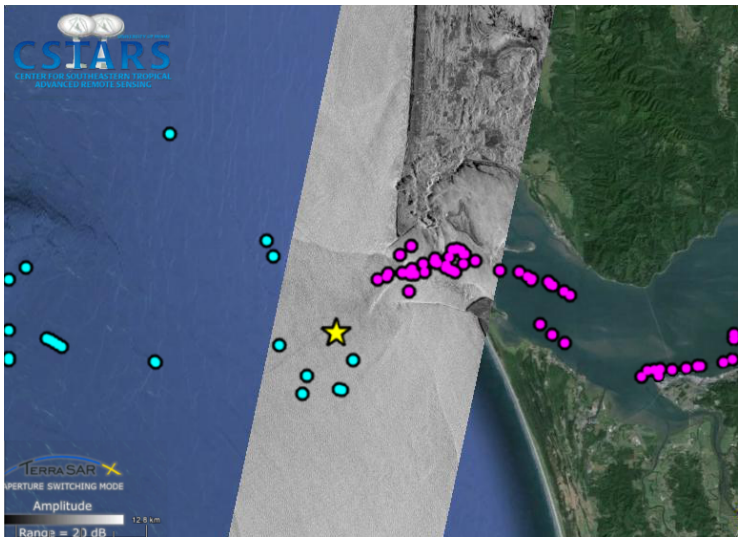

Figure 2. Map of MCR with data acquisition locations marked and a sample TerraSAR-X intensity image overlaid. SAR image was collected on 2 June 2013. Magenta dots represent those runs taken as inside the mouth; cyan dots represent those runs taken as outside the mouth. This color code will remain consistent throughout the figures presented here. The yellow star represents NDBC buoy #46243.

3. Results

For all values of wind speed and wind stress magnitude, k_p outside the inlet is smaller than k_p inside the inlet, with little observed wind sensitivity. The re-processed open-ocean results of [9] (figure 4) are also given for consideration; however, the inside-inlet values appear to be closest to those results. For higher wind speed values, a gravity-capillary regime peak (≈ 500 rad/m) appears for both outside and inside-inlet cases. These values are very close to those obtained from the stereoscopic observational spectra of Yurovskaya *et al*. [6]. The separation between k_p plotted against wind speed and k_p plotted against wind stress manifests itself in the existence of this high-wavenumber peak. This can be seen explicitly in the four spectra presented in figure 3: the example cases all have similar wind speed magnitudes, but those with low wind stress (3a, 3b) show a high-wavenumber peak. For the full body of the data set, figures 4a and 4b appear to mirror one another. As in figure 3, greater scatter in k_p and higher-wavenumber spectral peaks are associated with high wind speed and low wind stress. This disparity will be discussed in greater detail in section 4.

The spectral shape of the near-capillary regime (the high-wavenumber portion of the gravity-capillary regime) is shown in figure 5. The parameter n (i.e., $B(k) \sim k^n$) is plotted against wind speed U_{10} rather than wind stress magnitude τ so that the results from past observations [6, 9] can be shown in their native form in order to avoid invoking a wind stress parameterization. Whereas the spectra from [9] show good agreement with those of [6], those observed for this work are generally steeper, falling off like k^{-2}. None of the spectra shown have a discernable steepening or shallowing trend with wind speed, though there is a regime between $U_{10} = 7$ m/s and $U_{10} = 9$ m/s for which the scatter in outside-inlet spectral fall-off is greater, with some cases exhibiting $k^{-2.5}$ behavior.

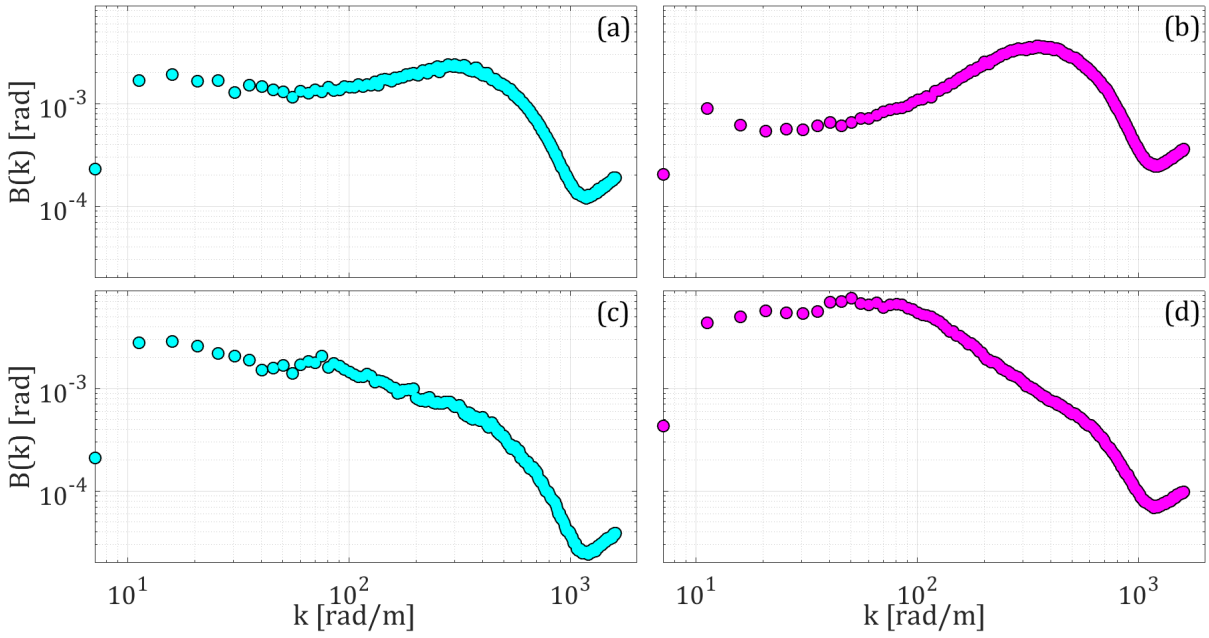

Figure 3. Four selected omnidirectional saturation spectra B(k). Magenta cases are inside-inlet. Cyan cases are outside-inlet. Wind conditions: (a) U_{10} = 7.879 m/s, τ = 0.0117 N/m^2; (b) U_{10} = 7.952 m/s, τ = 0.0688 N/m^2; (c) U_{10} = 8.548 m/s, τ = 0.139 N/m^2; (d) U_{10} = 8.476 m/s, τ = 0.102 N/m^2.

4. Discussion

Analysis of this Columbia River short wave and wind stress data set provides valuable observations of the shape and scale of the gravity-capillary and near-capillary regimes of the ocean wavenumber spectrum. The initial high value and tapering off of scatter in k_p as wind stress magnitude increases (shown in figure 4b) is an important part of this picture. In times of low wind forcing, feature interactions that might induce wave breaking (wave-wave, wave-geography, etc.) are likely to be significant drivers of variations in the position of the short wave spectral peak and the near-capillary regime shape. As wind forcing magnitude increases, the aforementioned interactions become secondary and the position of k_p moves almost exclusively into the short gravity wave regime. It is important to note that within the river inlet, waves grow over shorter fetches, ranging between 3 and 5 km in the regions sampled. The data shown in figure 4b is a graphical indication that sea states with high-wavenumber spectral peaks may exist in absence of significant wind stress magnitude and in sea states that have evolved over short distances. The spectra shown in figure 3 illustrate the connection between wind stress magnitude and k_p. The fact that "high" ($\approx$ 500 rad/m) wavenumber peaks all but disappear for the upper half of the wind stress magnitude range could be indicative of an increase in the lower-wavenumber (i.e., centimeter and decimeter-scale) features on the ocean surface that are relevant for the atmospheric turbulence used to estimate τ. A cursory look at 4a (i.e., k_p as a function of U_{10}) would not lead to this result, underlining the importance of computing wind stress during investigations of k_p.

In the examination of the near-capillary regime spectral shape (as in figure 5), one sees that the spectra observed here are steeper than those of prior observations [6, 9], though all share a similar, general insensitivity to wind speed. There exists no consensus in the body of capillary wave spectral data that suggests a clear expected behavior. Observational spectra [6, 9] that extend into the capillary or near-capillary regime are sparse, while empirical/parameterized spectra [13, 15] vary greatly in that domain, owing largely to the diverse range of observations and theoretical frameworks invoked in their construction [1, 13, 15].

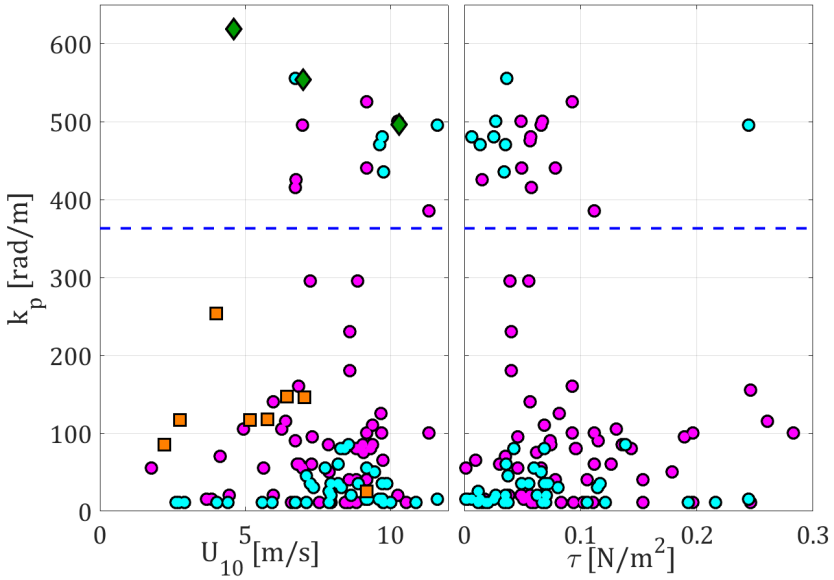

Figure 4. Peak wavenumbers of the omnidirectional saturation spectra, plotted against wind speed magnitude U_{10} (a) and wind stress magnitude τ (b). Magenta dots represent those runs taken as inside the mouth; cyan dots represent those runs taken as outside the mouth. The blue dashed line marks the wavenumber (370 rad/m) at which the gravity-capillary minimum phase speed (0.23 m/s) occurs. Green diamonds represent the peaks of the stereoscopic observational spectra of Yurovskaya *et al.* [6] and orange squares represent the peaks of the polarimetric observational spectra of Laxague *et al.* [9].

5. Conclusion

In summary, these results offer some insight to the subject of coastal air-sea interaction, and not only in the areas previously mentioned (remote sensing, etc.). The disparate behavior of k_p with respect to U_{10} and τ underscores the importance of short ocean waves in turbulent momentum flux. Geographic and spatial considerations likely figured heavily into these observations — the Columbia River mouth is unique in its interaction between highly energetic ocean-like conditions and river-like conditions in such close proximity and at such a grand scale. Background current and long wave effects have not been explicitly considered here, though their impact should be considered in future analysis of the data set. The estimates of near-capillary regime spectral shape do not form a significant result in their own right; however, they represent an important addition to the body of observational ocean surface short wave data. Future study in this vein would include the extension of surface roughness towards existing Columbia River satellite radar remote sensing acquisition, particularly with regard to hydrodynamic wave modulation. The use of these spectral shape measurements along with existing scattering models would allow the authors to independently evaluate NRCS from polarimetric slope data. Finally, it is only natural to dedicate more time and energy to better understanding the complex dynamics impacting short wave directionality. A more rigorous study of the factors affecting it, including wind speed/stress direction, long wave direction and current direction, follows directly from this work.

Acknowledgments

This research was supported by grant #N000141410643 from the Office of Naval Research and grant #SA1207GOMRI005 from BP/the Gulf of Mexico Research Initiative. Thanks are given to all those who worked on and prepared for our portion of the RIVET-II experiment, in particular Mike Rebozo. The authors are grateful to the captain and crew of the R/V *Point Sur* for their hard work and careful execution through conditions ranging from quiet to rough.

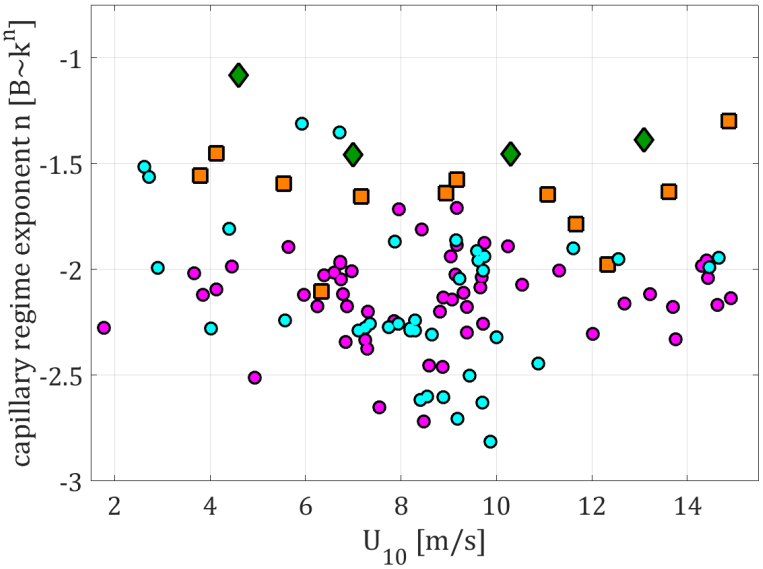

Figure 5. Near-capillary regime spectral shape exponent n (for $B(k) \sim k^n$), plotted against wind speed magnitude U_{10} for comparison with other observational spectra. Magenta dots represent those runs taken as inside the mouth; cyan dots represent those runs taken as outside the mouth. Green diamonds represent the shapes of the stereoscopic observational spectra of Yurovskaya *et al*. [6] and orange squares represent the shapes of the polarimetric observational spectra of Laxague *et al*. [9].

References

[1] Kudryavtsev V, Hauser D, Caudal G and Chapron B *Journal of Geophysical Research: Oceans* **108** ISSN 2156-2202
[2] Frew N M, Bock E J, Schimpf U, Hara T, Hauecker H, Edson J B, McGillis W R, Nelson R K, McKenna S P, Uz B M and Jähne B *Journal of Geophysical Research: Oceans* **109** ISSN 2156-2202
[3] Smith S D 1980 *J. Phys. Oceanogr.* **10** 18
[4] Charnock H 1955 *Q. J. R. Meteorol. Soc.* **81** 1
[5] Hara T, Bock E J and Lyzenga D *Journal of Geophysical Research: Oceans* **99** ISSN 2156-2202
[6] Yurovskaya M, Dulov V, Chapron B and Kudryavtsev V 2013 *Journal of Geophysical Research: Oceans* **118** 4380–4394
[7] Zappa C J, Banner M L, Schultz H, Corrada-Emmanuel A, Wolff L B and Yalcin J 2008 *Measurement Science and Technology* **19** 055503
[8] Zappa C J, Banner M L, Schultz H, Gemmrich J R, Morison R P, LeBel D A and Dickey T 2012 *Journal of Geophysical Research: Oceans (1978–2012)* **117**
[9] Laxague N J, Haus B K, Bogucki D and Özgökmen T 2015 *Journal of Geophysical Research: Oceans* **120** 3140–3156
[10] Anctil F, Donelan M A, Drennan W M and Graber H C 1994 *J. Atmos. Ocean. Technol.* **11** 7
[11] Ortiz-Suslow D, Haus B, Williams N, Laxague N, Reniers A and Graber H 2015 *Journal of Geophysical Research: Oceans* **120** 660–676
[12] Millard R and Seaver G 1990 *Deep Sea Research Part A. Oceanographic Research Papers* **37** 1909–1926
[13] Elfouhaily T, Chapron B, Katsaros K and Vandemark D 1997 *Journal of Geophysical Research-Oceans* **102** 15781–15796
[14] Kudryavtsev V, Makin V and Chapron B 1999 *J. Geophys. Res* **104** 7369
[15] Hwang P A, García-Nava H and Ocampo-Torres F J 2011 *J. Phys. Oceanogr.* **41** 1227–1238